

Original Research

Analysis of Unstable Hydrofoil Energy-Capturing Motion Due to Energy Dissipation

Yudong Xie^{1,2*}, Chen Chen^{1,2}, Yong Wang^{1,2}, Penglei Ma^{1,2}, Jianwei Lu^{1,2}

¹School of Mechanical Engineering, Shandong University, Shandong, China

²Key Laboratory of High-Efficiency and Clean Mechanical Manufacture, Ministry of Education, Shandong, China

Received: 1 September 2017

Accepted: 22 October 2017

Abstract

As energy crises and environmental pollution become increasingly prominent, people are beginning to explore the ocean to exploit its renewable energy. Based on hydrodynamic principles, an analytical model for unstable hydrofoil motion has been developed. The software ANSYS Fluent was employed to perform a simulation of hydrofoil motion, and the effect of hydrofoil motion on the surrounding flow field was analyzed. The hydrodynamic characteristics and energy-capturing efficiency of the hydrofoil were obtained, and the influence of complex flows on hydrofoil hydrodynamics was elucidated. The energy dissipation mechanism during hydrofoil motion was characterized. The results indicate that the vortex generation and shedding inevitably dissipates part of the tidal energy captured by the hydrofoil, which leads to abrupt changes in hydrofoil hydrodynamics and reduces energy-capturing efficiency. When the frequency of the abrupt hydrodynamics change matches the hydrofoil natural frequency, it may result in hydrofoil resonance and damage. Also, it is observed that larger pitch amplitude leads to larger optimal-reduced frequency corresponding to the peak power cycle-averaged coefficient. The results also provide a theoretical guide on how to improve hydrofoil energy-capturing efficiency of the power generation system with control valves and extend hydrofoil life.

Keywords: tidal energy, power, environmental protection, energy dissipation, control valve

Introduction

Energy is essential to human survival and development. Currently, conventional fossil fuels are being depleted, and the environment is deteriorating [1-2]. As the energy crisis and environmental pollution become increasingly prominent, people are beginning to explore the ocean to exploit its abundant reserve of renewable energy [3-4].

Tidal energy is one form of renewable energy in the ocean [5-7]. Fig. 1 illustrates a design to capture tidal energy via hydrofoil oscillation. U is the far-field free incoming flow velocity, LE is the hydrofoil leading edge point, TE is the hydrofoil trailing edge point, and X_p is the distance between the pitch axis and the leading edge point LE. The variable angle system of attack controls the hydrofoil rotation around the pitch axis (pitching motion (θ)). Affected by the tides, the fluid force on the hydrofoil includes the lift force $F(t)$, drag force $D(t)$ and pitch moment $M(t)$. Affected by $F(t)$, the hydrofoil undergoes cyclic vertical ascending and descending motions (heaving motion $z(t)$). Because the hydrofoil

*e-mail: ydxie@sdu.edu.cn

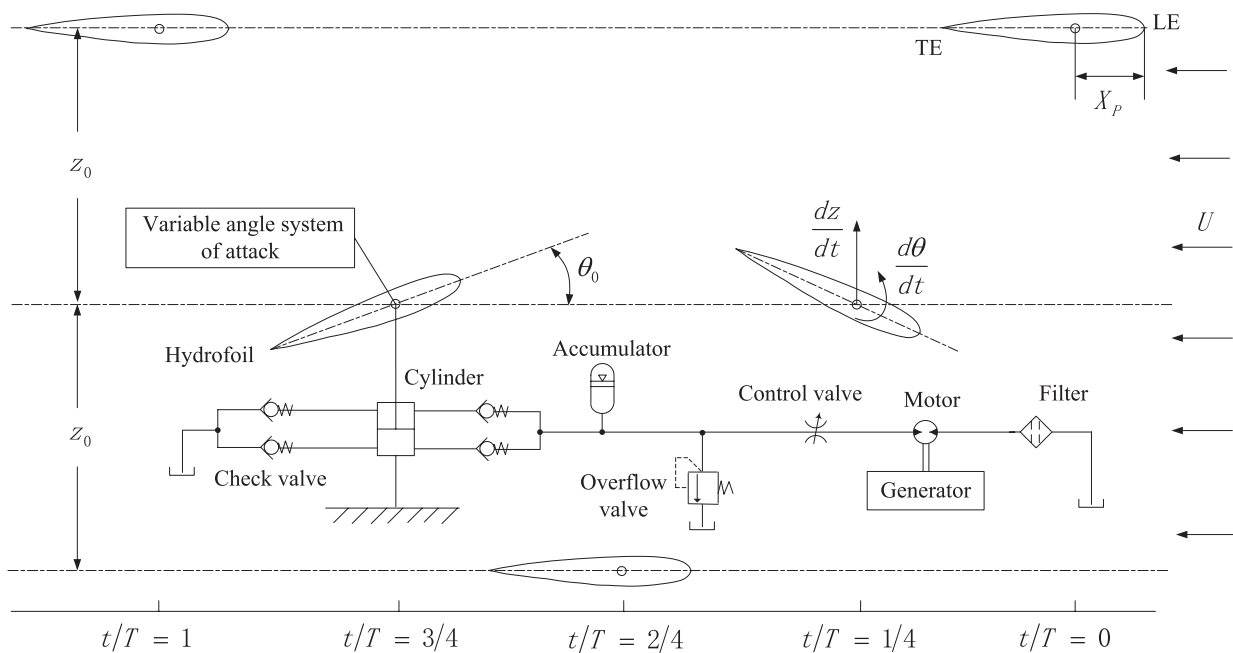


Fig. 1. Hydrofoil oscillation in a cycle.

is prohibited from undergoing horizontal motion, hydrofoil oscillation is treated as a coupling of pitch motion $\theta(t)$ and heaving motion $z(t)$. In Fig. 1, θ_0 is the pitch amplitude, Z_0 is the heaving amplitude, $d\theta/dt$ is pitch velocity, and dz/dt is heaving velocity. We assume that the laws for hydrofoil pitch motion $\theta(t)$ and heaving motion $z(t)$ are, respectively, obtained from the following expressions:

$$\theta(t) = \theta_0 \sin(2\pi ft + \alpha_1) \quad (1)$$

$$z(t) = z_0 \sin(2\pi ft + \alpha_2) \quad (2)$$

...where f is the oscillation frequency and α_1 and α_2 are the initial phases of pitch motion and heaving motion, respectively.

As shown in Fig. 1, under oscillatory motion, the hydrofoil constantly captures kinetic energy from the incoming flow and drives a cylinder to generate high-pressure oil in the power generation system with control valves. The high-pressure oil rotates a hydraulic motor, and the motor drives a generator to generate electricity. Compared with a conventional plan that leverages a vertical or horizontal axis water turbine to capture tidal energy, the plan shown in Fig. 1 has the following advantages: the horizontal hydrofoil dimension is unrestricted by water depth, and the effective hydrofoil energy absorption area to capture tidal energy can be relatively large; therefore, the power generation equipment has a low start-up flow velocity and high single equipment power generation capacity.

To capture tidal energy efficiently, many researchers have studied the hydrofoil's hydrodynamic performance [8-11]. McKinney et al. first proposed the concept of capturing energy in a fluid via an oscillating wing [12].

Jones et al. studied the energy-capturing efficiency of an oscillating wing at various pitch amplitudes and reached the conclusion that an oscillating wing is superior to a rotational water turbine in capturing energy from shallow water [13]. Fenercioglu et al. investigated vortical flow structures around and in the wake of an oscillating NACA0012 airfoil [11]. Amiralaie et al. investigated the effect of an oscillating wing's non-steady parameters on its dynamic characteristics under low Reynolds numbers [14-15]. Thiery et al. investigated the effect of turbulence model on the predicted energy-capturing efficiency [16-17]. Ashraf and Young et al. investigated the effect of factors such as the hydrofoil motion trajectory, pitch-heaving phase difference, and hydrofoil parameters on energy-capturing efficiency [18-19]. Benramdane et al. [20] performed time-frequency analysis of wall pressure signals of a hydrofoil's suction side undergoing a forced transient pitching motion with incoming flow. Ghasemi et al. [21-22] developed a two-dimensional and three-dimensional computational tool to study a baseline simulation of tethered undersea kite systems. Sagharichi et al. [23] used the method of computational fluid dynamics to analyze the unsteady two-dimensional flow simulation, and the simulations show that the variable-pitch blade turbine can reduce or eliminate the flow separation on its blades. Zhu [24] conducted a numerical study to examine the correlation between wake instability and energy harvesting performance of a flapping foil, and the results show that effective angle of attack is more physically relevant due to its close correlation with leading edge separation. Shimizu et al. [25] employed optimization algorithms based on two-dimensional Navier–Stokes solutions to explore the performance of a semi-activated system. Young et al. [26] investigated the progress in analytical

and computational studies, lab-based and small-scale experiments, and large-scale industrial development. The results show that the highest levels of power and efficiency are associated with very large foil pitch angles (upwards of 70°) and angles of attack (30-40°).

Ever since these pioneering studies, an important focus has been to identify the optimal combination of kinematic parameters of the hydrofoil [27]. So far, little attention has been given to studying the energy dissipation mechanism during the hydrofoil energy-capturing process. In this paper, an unstable hydrofoil oscillation model was created to carry out research on various aspects such as motion, stress, energy absorption, and flow field. The mechanism of energy dissipation during hydrofoil motion was explained.

Methods

Hydrofoil Instability Analysis Model

The hydrofoil sits underwater at a depth of h ; its shape is symmetric, and its coordinates are shown in Fig. 2. The hydrofoil chord length is c . The incoming flow velocity is U . The hydrofoil can be idealized as a thin wing whose thickness is small compared with the span and chord length. So, the hydrofoil's hydrodynamic properties can be calculated via Airy wave theory.

According to hydrodynamic principles [6, 11], we assume that the hydrofoil surface displacement equation is $f_L(x, y, t)$:

$$f_L(x, y, t) = \Theta(x, y)e^{i\omega t} \tag{3}$$

We also assume that the fluid is an incompressible fluid and that the motion is irrotational; thus, the velocity potential satisfies the Laplace equation:

$$\nabla\Phi = 0 \tag{4}$$

The free water surface condition is as follows [28]:

$$g \frac{\partial\Phi}{\partial z} \Big|_{z=h} + \left(\frac{\partial\Phi}{\partial t} - U \frac{\partial\Phi}{\partial x}\right)^2 \Big|_{z=h} = 0 \tag{5}$$

The velocity potential satisfies the radiation condition at infinite distance and satisfies the disturbance-free condition at infinite depth [29]; additionally, the hydrofoil surface satisfies the following equation [28-31]:

$$\mathcal{R}(x, y, t) = \frac{\partial\Phi}{\partial z} \Big|_{z=0} = \frac{\partial f_L(x, y, t)}{\partial t} - U \frac{\partial f_L(x, y, t)}{\partial x} \tag{6}$$

The unsteady vortex system on the hydrofoil surface S is $\Gamma(\varepsilon, \gamma)e^{i\omega t}$. In unbounded flow, the vortex system is replaced by a dipole [29-30], and the microelement-bound vortex system velocity potential is represented by the velocity potential of the bound microelement dipole system [28-30]:

$$\Phi_a = -\frac{1}{4\pi} e^{i\omega t} \Gamma(\varepsilon, \gamma) \frac{\partial N}{\partial z} \tag{7}$$

...where
$$N = \frac{1}{\sqrt{(x-\varepsilon)^2 + (y-\gamma)^2 + z^2}}$$

In a bound vortex downstream, a free vortex extends along the negative direction of the x axis. Similarly, the free vortex system is replaced by a free dipole system [28]. The free dipole system created by the bound dipole at $(\varepsilon, \gamma, 0)$ distributes from ε along the negative direction of the x axis toward $-\infty$. Its strength at $(v, \gamma, 0)$ is as follows [28-30]:

$$\Phi_b = -\frac{1}{4\pi} e^{i\omega t_1} \Gamma(\varepsilon, \gamma) \frac{\partial N_1}{\partial z} \tag{8}$$

... where $t_1 = t - \frac{\varepsilon-v}{U}$,

$$N_1 = \frac{1}{\sqrt{(x-v)^2 + (y-\gamma)^2 + z^2}}$$

To facilitate analysis of the vortex system strength, the following transformation is introduced [28-32]:

$$\begin{cases} \lambda = x - (v - \varepsilon) \\ d\lambda = -dv \end{cases} \tag{9}$$

According to hydrodynamic principles, the velocity potential of the entire unsteady vortex system is as follows [6, 28-30]:

$$\begin{aligned} \check{\Phi} = & -\frac{e^{i\omega t}}{8\pi^2} \int_S \Gamma(\varepsilon, \gamma) d\varepsilon d\gamma \int_{-\infty}^{\varepsilon} e^{i\bar{\omega}(v-\varepsilon)} dv \frac{\partial N_2}{\partial z} \end{aligned} \tag{10}$$

...where $\bar{\omega} = \frac{\omega}{U}$,

$$N_2 = \int_{-\pi}^{\pi} \int_0^{\infty} e^{-\lambda z + i\lambda(x-v) \cos u + i\lambda(y-\gamma) \sin u} d\lambda du$$

The vortex system strength $\Gamma(\varepsilon, \gamma)$ is calculated from the hydrofoil surface boundary condition as follows [28, 31-32]:

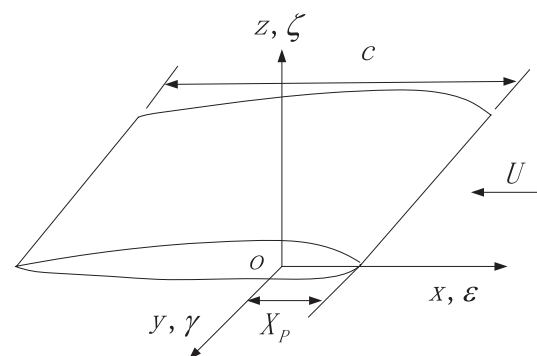


Fig. 2. Decomposition of hydrofoil coordinates.

$$\begin{aligned}
\frac{\partial \Phi}{\partial z} \Big|_{z=0} = & \frac{1}{8\pi} e^{i\omega t} \int_S \Gamma(\varepsilon, \gamma) \cdot \left[\int_{-\frac{\pi}{2}}^{\frac{\pi}{2}} \frac{\omega^2}{\cos^3 u} e^{\frac{\overline{\omega}(x_0 \cos u + y_0 \sin u)}{\cos u}} du \right] d\varepsilon d\gamma \\
& - \frac{1}{8\pi^2} e^{i\omega t} \int_S \Gamma(\varepsilon, \gamma) \cdot \left[\int_{-\pi}^{\pi} \int_0^{\infty} \frac{i\lambda^2 e^{i\lambda(x_0 \cos u + y_0 \sin u)}}{\lambda \cos u - \overline{\omega}} d\lambda du \right] d\varepsilon d\gamma \\
& - \frac{1}{8\pi^2} e^{i\omega t} \int_S \Gamma(\varepsilon, \gamma) \cdot \left[\lim_{z \rightarrow 0} \int_{-\pi}^{\pi} \int_0^{\infty} \frac{i\lambda^2 e^{\lambda(-z + ix_0 \cos u + iy_0 \sin u)}}{\lambda \cos u - \overline{\omega}} d\lambda du \right] d\varepsilon d\gamma \\
& - \frac{1}{8\pi} e^{i\omega t} \int_S \Gamma(\varepsilon, \gamma) \cdot \left[\lim_{z \rightarrow 0} \int_{-\frac{\pi}{2}}^{\frac{\pi}{2}} \frac{\omega^2}{\cos^3 u} e^{\frac{\overline{\omega}(-z + ix_0 \cos u + iy_0 \sin u)}{\cos u}} du \right] d\varepsilon d\gamma \\
& + \frac{1}{4\pi} e^{i\omega t} \int_S \Gamma(\varepsilon, \gamma) \cdot \left[\int_{-\frac{\pi}{2}}^{\frac{\pi}{2}} \frac{\delta_1^3 e^{i\delta_1(x_0 \cos u + y_0 \sin u)}}{(\overline{\omega} - \delta_1 \cos u) \sqrt{1 + 4\beta \cos u}} du \right] d\varepsilon d\gamma \\
& - \frac{1}{4\pi} e^{i\omega t} \int_S \Gamma(\varepsilon, \gamma) \cdot \left[\int_{-\frac{\pi}{2}}^{\frac{\pi}{2}} \frac{\delta_1^3 e^{i\delta_1(x_0 \cos u + y_0 \sin u)}}{(\overline{\omega} - \delta_1 \cos u) \sqrt{1 + 4\beta \cos u}} du \right] d\varepsilon d\gamma \\
& + \frac{1}{4\pi} e^{i\omega t} \int_S \Gamma(\varepsilon, \gamma) \cdot \left[\int_{-\pi}^{\pi} \frac{\delta_2^3 e^{i\delta_2(x_0 \cos u + y_0 \sin u)}}{(\overline{\omega} - \delta_2 \cos u) \sqrt{1 + 4\beta \cos u}} du \right] d\varepsilon d\gamma \\
& + \frac{1}{4\pi^2} e^{i\omega t} \int_S \Gamma(\varepsilon, \gamma) \cdot \left[\int_{-\pi}^{\pi} \int_0^{\infty} \frac{\lambda \overline{\omega} e^{i\lambda(x_0 \cos u + y_0 \sin u)}}{(\lambda \cos u - \overline{\omega}) \cos u} d\lambda du \right] d\varepsilon d\gamma \\
& - \frac{1}{4\pi^2} e^{i\omega t} \int_S \Gamma(\varepsilon, \gamma) \cdot \left[\int_{-\pi}^{\pi} \int_0^{\infty} \frac{\lambda \delta_1^2 e^{i\lambda(x_0 \cos u + y_0 \sin u)}}{(\lambda - \delta_1)(\delta_1 \cos u - \overline{\omega}) \sqrt{1 + 4\beta \cos u}} d\lambda du \right] d\varepsilon d\gamma \\
& + \frac{1}{4\pi^2} e^{i\omega t} \int_S \Gamma(\varepsilon, \gamma) \cdot \left[\int_{-\pi}^{\pi} \int_0^{\infty} \frac{\lambda \delta_2^2 e^{i\lambda(x_0 \cos u + y_0 \sin u)}}{(\lambda - \delta_2)(\delta_2 \cos u - \overline{\omega}) \sqrt{1 + 4\beta \cos u}} d\lambda du \right] d\varepsilon d\gamma
\end{aligned} \quad (11)$$

...where $\beta = \frac{\omega U}{g}$, $\delta_1 = \frac{g(1+2\beta \cos u + \sqrt{1+4\beta \cos u})}{2U^2 \cos^2 u}$, $\delta_2 = \frac{g(1+2\beta \cos u - \sqrt{1+4\beta \cos u})}{2U^2 \cos^2 u}$, $x_0 = x - \varepsilon$, and $y_0 = y - \gamma$.

Assume that $\eta = \frac{\omega c}{2U}$, $\sigma = \frac{2h}{c}$, $\tau = \frac{U}{\sqrt{gh}}$, \mathcal{L} is a function of η , $\mathcal{L} = \mathcal{L}(\eta)$; \mathcal{H} is a function of η and σ , $\mathcal{H} = \mathcal{H}(\eta, \sigma)$; and Ψ is a function of η , σ , and τ , and $\Psi = \Psi(\eta, \sigma, \tau)$. Then in formula (11) the first and second items are functions of \mathcal{H} ; the third and the fourth items are functions of \mathcal{L} ; and the remaining items are functions of Ψ . Therefore, formula (11) can be represented in dimensionless form as follows [28-32]:

$$\begin{aligned}
\frac{1}{U} \frac{\partial \Phi}{\partial z} \Big|_{z=0} = & \frac{e^{i\omega t}}{4\pi U} \int_S \Gamma(\varepsilon, \gamma) [\mathcal{L}(\eta) \\
& + \mathcal{H}(\eta, \sigma) + \Psi(\eta, \sigma, \tau)] d\varepsilon d\gamma \quad (12)
\end{aligned}$$

Assume that the hydrofoil surface displacement comprises n modals $f_{Lj}(x, y)$ ($j = 1, 2, \dots, n$), then the hydrofoil surface velocity of the j -th modal is calculated via formula (6) [28]:

$$\mathcal{R}_j(x, y, t) = \frac{\partial f_{Lj}(x, y, t)}{\partial t} - U \frac{\partial f_{Lj}(x, y, t)}{\partial x} \quad (13)$$

$$\begin{aligned}
\overline{\mathcal{R}_j}(x, y) e^{i\omega t} = & [i\omega \overline{f_{Lj}}(x, y) \\
& - U \overline{f_{Ljx}}(x, y)] e^{i\omega t} \quad (14)
\end{aligned}$$

Based on equation (12), the integral equation of the corresponding vortex distribution $\Gamma_j(\varepsilon, \gamma)$ is calculated as follows [28-30]:

$$\begin{aligned}
\frac{1}{U} \overline{\mathcal{R}_j}(x, y) = & \frac{1}{4\pi U} \int_S \Gamma_j(\varepsilon, \gamma) [\mathcal{L}(\eta) \\
& + \mathcal{H}(\eta, \sigma) + \Psi(\eta, \sigma, \tau)] d\varepsilon d\gamma \quad (15)
\end{aligned}$$

The integral equation (15) for $j = 1, 2, \dots, n$ is solved to obtain the corresponding bound vortex distribution $\Gamma_j(\varepsilon, \gamma)$. The lift force distribution on the hydrofoil surface is as follows [28]:

$$F_j = \rho U \Gamma_j(\varepsilon, \gamma) \quad (16)$$

...where ρ is fluid density.

The hydrofoil wall boundary is divided into m element surfaces. At moment t element surface i in the incoming flow direction is $\overline{\sigma}_{i-x}(t)$, the force vertical to the incoming flow direction is $\overline{\sigma}_{i-z}(t)$; the projection of distance from the center of the element surface i to the pitch axis in the x direction is $d_{i-x}(t)$; the projection of distance from the element surface center i to the pitch axis in the z direction is $d_{i-z}(t)$. The moment of force on element surface i versus the pitch axis can be calculated as follows:

$$M_i(t) = \overline{\sigma}_{i-x}(t) d_{i-z}(t) + \overline{\sigma}_{i-z}(t) d_{i-x}(t) \quad (17)$$

The directions of the buoyancy and gravity of the hydrofoil are opposite. In this paper, hydrofoil buoyancy is equal to its gravity. $F(t)$, $D(t)$, and $M(t)$ on the hydrofoil are:

$$F(t) = \sum_{i=1}^m \overline{\sigma}_{i-z}(t) \quad (18)$$

$$D(t) = \sum_{i=1}^m \overline{\sigma}_{i-x}(t) \quad (19)$$

$$M(t) = \sum_{i=1}^m M_i(t) \quad (20)$$

The power captured by the hydrofoil from incoming flow is as follows:

$$P(t) = F(t) \frac{dz(t)}{dt} + M(t) \frac{d\theta(t)}{dt} \quad (21)$$

The hydrofoil surface displacement Equation (3) is represented by the vibration modal as follows [28-30]:

$$f_L(x, y, t) = \sum_{r=1}^n \overline{f_{Lr}}(x, y) \overline{\theta}_r(t) \quad (22)$$

...where $\overline{\theta}_r(t)$ is a general coordinate. In the case of simple harmonic vibration with frequency ω , the hydrofoil surface of the r -th modal is:

$$\overline{\mathcal{R}}_r(x, y) e^{i\omega t} = [i\omega \overline{f_{Lr}}(x, y) - U \overline{f_{Lrx}}(x, y)] e^{i\omega t} \quad (23)$$

Based on the integral equation (15), the corresponding vortex distribution $\Gamma_r(\varepsilon, \gamma)$ is calculated. Based on equation (16), the corresponding lift force distribution $F_r(x, y)$ is calculated. The general force corresponding to the r -th general coordinate is as follows [30-32]:

$$\begin{aligned} \Omega_r(t) &= \int_S \sum_{j=1}^n F_j(\varepsilon, \gamma) \overline{f_{Lr}}(\varepsilon, \gamma) e^{i\omega t} d\varepsilon d\gamma \\ &= \sum_{j=1}^n (\omega^2 \Delta_{rj} - i\omega \Lambda_{rj} - \Pi_{rj}) e^{i\omega t} \end{aligned} \quad (24)$$

...where matrices Δ_{rj} , Λ_{rj} , Π_{rj} are functions of the dimensionless variables η , σ , τ .

In formula (24), Λ_{rj} arises from vortex dissipation of the energy captured by the hydrofoil. Greater vortex energy dissipation implies lower hydrofoil tidal energy-capturing efficiency. Additionally, as it contains a linear component and a rotational non-linear component of the fluid mainstream, this effect leads to an abrupt change phenomenon in the variation of the hydrofoil lift force, resistance, and power. To facilitate analysis of the effect of these variations on hydrofoil hydrodynamic performance, expressions [21] for the instantaneous lift coefficient $C_l(t)$, instantaneous drag coefficient $C_d(t)$, instantaneous pitch moment coefficient $C_m(t)$, instantaneous power coefficient $C_p(t)$, power cycle-averaged coefficient $\overline{C}_p(t)$, and power extraction efficiency η are defined as follows:

$$C_l(t) = \frac{2F(t)}{\rho U^2 c} \quad (25)$$

$$C_d(t) = \frac{2D(t)}{\rho U^2 c} \quad (26)$$

$$C_m(t) = \frac{2M(t)}{\rho U^2 c^2} \quad (27)$$

$$C_p(t) = \frac{2P(t)}{\rho U^3 c} \quad (28)$$

$$\overline{C}_p = \frac{1}{T} \int_0^T C_p(t) dt \quad (29)$$

$$\eta = \frac{\frac{1}{T} \int_0^T P(t) dt}{\frac{1}{2} \rho U^3 H} \quad (30)$$

...where T is the oscillation period and H represents the swept area of the hydrofoil. H is the vertical displacement of the hydrofoil motion in a two-dimensional hydrofoil.

Hydrofoil hydrodynamic performance can be evaluated effectively via $C_l(t)$, $C_d(t)$, $C_m(t)$, $C_p(t)$, \overline{C}_p , and η . This evaluation is elaborated upon in the next section.

Numerical Simulation

In this section, the software ANSYS Fluent is employed to calculate the flow field during hydrofoil oscillation. In the simulation, the dynamic grid technique and the user-defined function are employed to complete the hydrofoil wall boundary oscillation simulation. The grid model for the fluid calculation area is shown in Fig. 3. A circular slip interface divides the square fluid calculation area into two parts, and physical variables on both sides are exchanged via the slip interface. The centers of both parts are on the hydrofoil pitch axis. The turbulence model employed is the Spalart-Allmaras model. The pressure and velocity coupling is based on a pressure implicit with splitting of operators (PISO) scheme. The absolute convergence standard for continuity and velocity residuals is 10^{-5} . In the model, the hydrofoil type is an NACA0015 symmetric hydrofoil, and fluid flows from left to right.

In order to ensure the independence of the numerical results with grid mesh resolution, numerical simulations were conducted using three different mesh cell sizes.

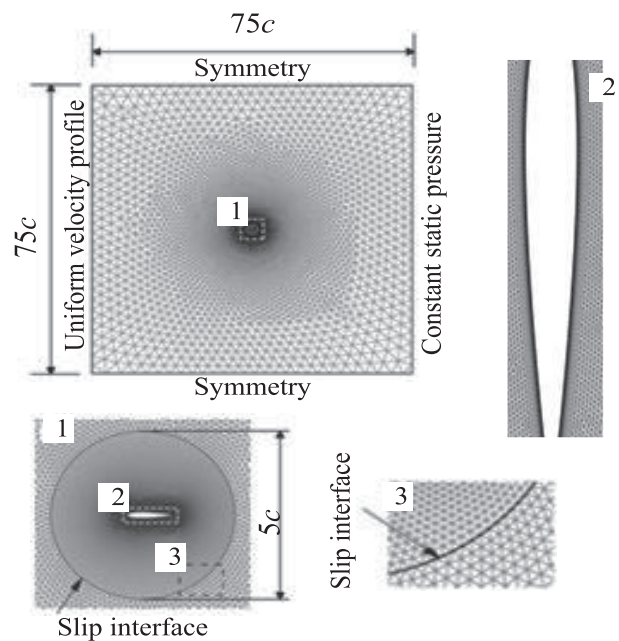


Fig. 3. Grid model.

Table 1. Grid and time step independence study.

Mesh cell number	Number of time steps/cycle	\bar{C}_p	$\eta/\%$
72,000	800	0.978	38.4
72,000	1,600	0.984	38.6
72,000	3,200	0.983	38.5
36,000	1,600	0.979	38.4
72,000	1,600	0.984	38.6
114,000	1,600	0.981	38.4

To verify the independence of solutions on the time step, simulations were done using three different time steps. The details of the study are shown in Table 1.

As can be seen in Table 1, the difference between the results with different levels of grid and time step refinement becomes negligible. To reduce computational time, the subsequent simulations have been performed using 72,000 mesh cells and 1,600 time steps per cycle.

Results and Discussion

In the simulations, the initial phase of the pitch motion is equal to 0, the pitch motion law is $\theta(t) = \theta_0 \sin(2\pi ft)$, and the heaving motion law is $z(t) = z_0 \sin(2\pi ft + \alpha_2)$, where $\theta_0 = 70^\circ$, $f = 0.24$ Hz, $z_0 = 0.8$ m, $\alpha_2 = 90^\circ$, $\frac{x_p}{c} = \frac{1}{3}$ the viscosity $\nu = 1 \times 10^{-6} \text{m}^2/\text{s}$, and the Reynolds number is $1,28 \times 10^6$. After the numerical simulation stabilizes, in the 4th oscillation cycle the vortex around the hydrofoil is shown in Fig. 4. And the pressure distribution of flow

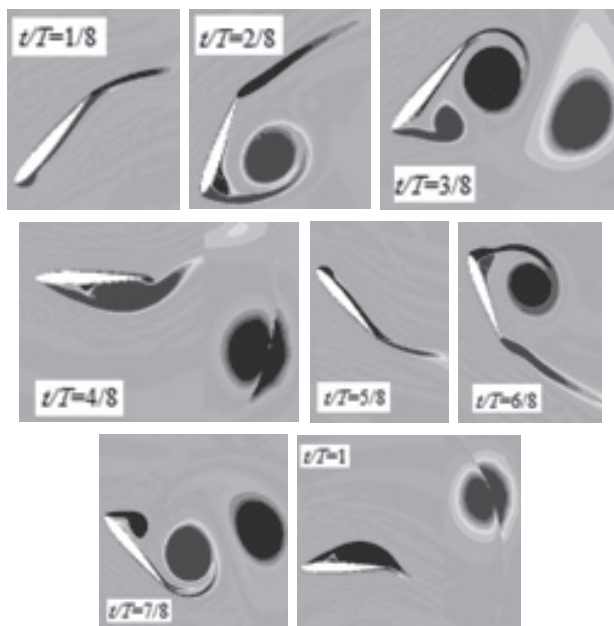


Fig. 4. Vortex contours.

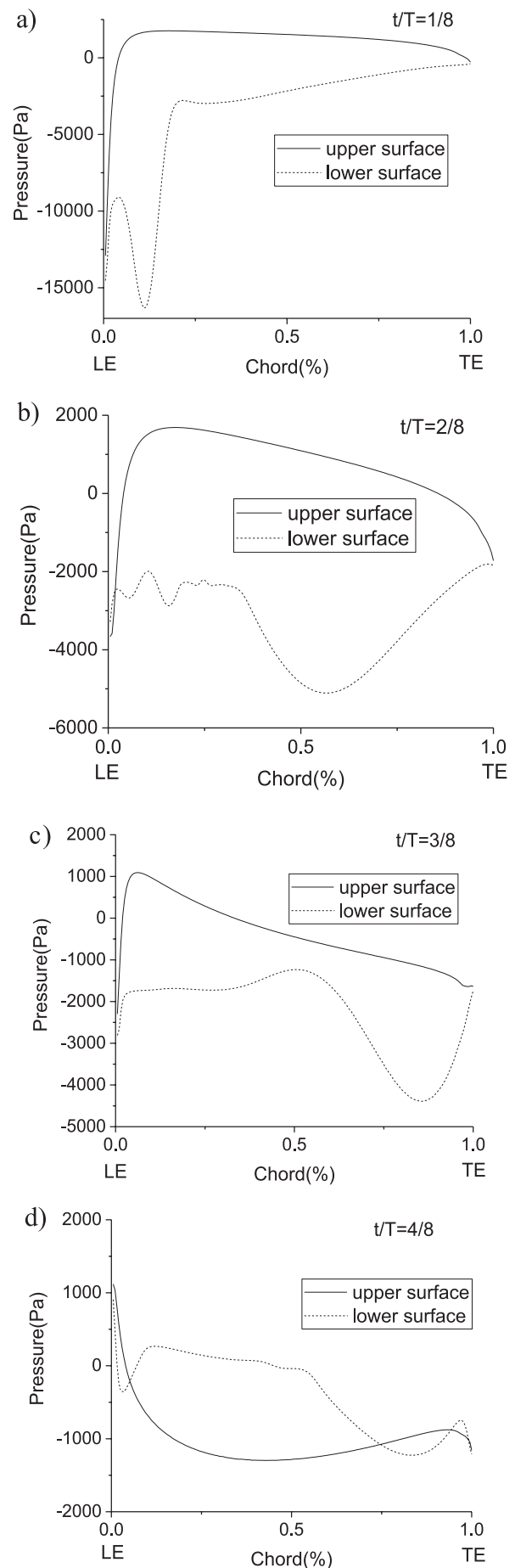


Fig. 5. Pressure distribution.

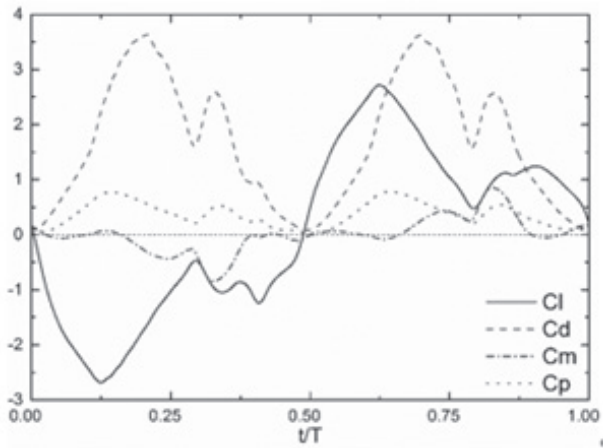


Fig. 6. Variation curves in a cycle.

field in the first half of the cycle is shown in Fig. 5. Fig. 6 shows variation curves of the coefficients in a cycle.

At $t/T = 1/8$, a small vortex (marked as I) appears at the leading edge point on the hydrofoil lower surface. The maximum pressure variation in the leading edge point area on the lower surface reaches 13,000 Pa. During the interval from 0 to 0.125 T, both the hydrofoil instantaneous lift coefficient $|C_l(t)|$ and instantaneous drag coefficient $C_d(t)$ are increasing; however, they have unstable and unequal increasing rates. Formulae (17)-(20) and formulae (25)-(27) indicate that the instantaneous pitch moment $M(t)$ is related to the instantaneous lift force $F(t)$ and instantaneous drag force $D(t)$, as well as to the rotational force arms of $F(t)$ and $D(t)$ versus the pitch axis. Affected by the variation of $|C_l(t)|$ and $C_d(t)$, the instantaneous pitch moment coefficient $C_m(t)$ fluctuates. Because vortex I is not fully formed, the energy dissipation is low; therefore, in the interval of 0 to 0.125 T, the instantaneous power $C_p(t)$ coefficient increases stably.

Subsequently, the hydrofoil continues its downward motion, and vortex I continues to grow. At $t/T = 2/8$, the main body of vortex I has shed from the hydrofoil. At the same time, a small vortex (marked as II) emerges in the hydrofoil lower surface area. With the shedding of vortex I and the formation of vortex II, the pressure variation is substantial, and oscillation shock occurs. During the interval from 0.125 T to 0.25 T, vortex shedding and generation inevitably dissipates part of the energy captured by the hydrofoil. Consequently, the instantaneous lift coefficient $|C_l(t)|$ drops from 2.7 to 1.0, the instantaneous drag coefficient $C_d(t)$ drops from 3.6 to 2.8, and the instantaneous power coefficient $C_p(t)$ starts to decline. This result indicates that the hydrofoil energy-capturing efficiency is declining.

Next, the hydrofoil continues its downward motion, and vortex I starts to move away from the hydrofoil lower surface. Simultaneously, a new vortex (marked as III) emerges around the hydrofoil leading edge point, while vortex II gradually grows. At $t/T = 3/8$, vortex II sheds from the hydrofoil trailing edge point.

From 0.25 T to 0.375 T, the vortex continues to grow, the instantaneous coefficients continue to decline, and oscillation shock occurs.

At $t/T = 4/8$ the hydrofoil moves to the lowest point, and no new vortices form. The pressure difference between the hydrofoil upper and lower surfaces decreases. At the lowest point, when the hydrofoil attack angle decreases, the instantaneous coefficients decline rapidly. The hydrofoil energy-capturing efficiency drops to the lowest level in a cycle.

After $t/T = 4/8$ the hydrofoil starts to move upward. In the second half of the cycle (0.5T-T), the flow field variation on the hydrofoil upper surface is similar to that on the lower surface in the first half of the cycle (0-0.5T), and the flow field variation on the hydrofoil lower surface is similar to that on the upper surface in the first half of the cycle (0-0.5T). Because vortex shedding is accompanied by dynamic stall, the hydrofoil dynamic performance deteriorates, which results in abrupt changes and oscillation shocks of the variation curves of the coefficients.

In a complete cycle T , when the hydrofoil extracts energy from the tide and converts it to mechanical energy, it also applies work to the fluid and converts hydrofoil mechanical energy to fluid turbulence kinetic energy. Because the hydrofoil mechanical energy originates from the tide, more fluid vortices and larger vortices around the hydrofoil results in more energy dissipation. This change leads to lower hydrofoil energy-capturing efficiency, which matches the law revealed by the aforementioned instability analysis model. In engineering practice, when the frequency of the abrupt change in the hydrodynamic force matches the hydrofoil natural frequency, it will result in hydrofoil resonance. Therefore, normal variation curves of the coefficients are desirably smooth to prevent hydrofoil oscillation shock. In the design of the energy power generation system, how to make the variation curves of these coefficients smooth becomes a key problem.

To facilitate analysis of the oscillation frequency effect of the hydrofoil on the oscillation shock and energy dissipation, dimensionless reduced frequency is defined as [22]:

$$f^* = \frac{fc}{U} \quad (31)$$

The power cycle-averaged coefficient, $\overline{C_p}(t)$, versus f^* , for the hydrofoil with different parameters are shown in Fig. 7. Fig. 7 shows that when the pitch and heaving amplitudes are fixed, $\overline{C_p}(t)$ initially increases monotonically with $\overline{C_p}(t)$. After reaching the maximum value, $\overline{C_p}(t)$ decreases rapidly if f^* is further increased. Additionally, it is seen that larger pitch amplitude θ_0 leads to larger optimal reduced frequency corresponding to the peak power cycle-averaged coefficient. For example, in the case of $\theta_0 = 60^\circ$ the optimal reduced frequency f^* is 0.10, while for $\theta_0 = 90^\circ$ the optimal reduced frequency f^* is 0.22.

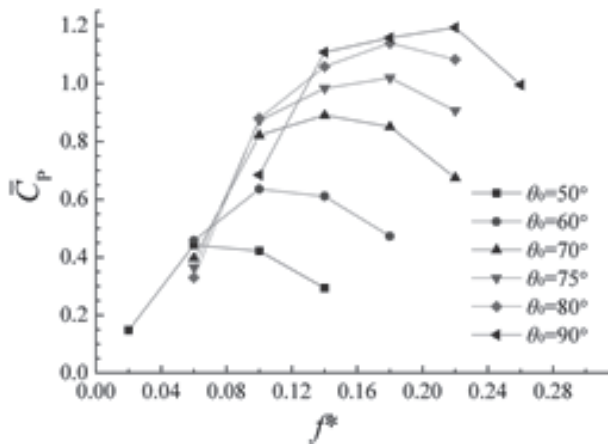
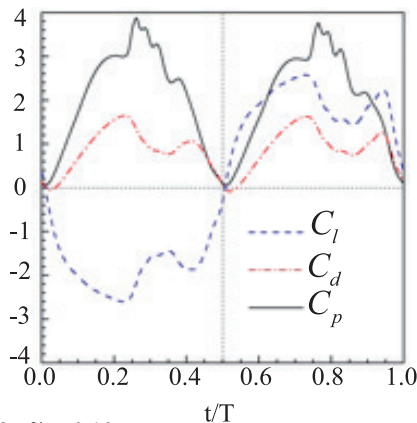
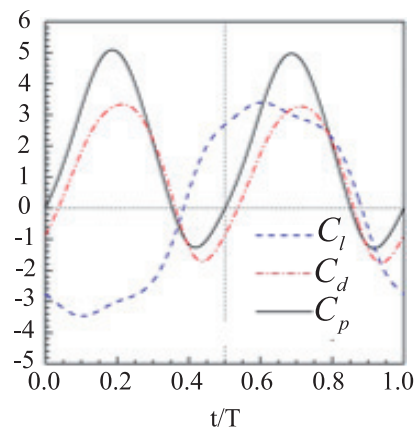


Fig. 7. Power cycle-averaged coefficient versus time between numerical simulations using different parameters ($X_p/c = 1/3$, $z_0/c = 1$, $U = 2.0$ m/s, $Re = 500,000$).

Fig. 8 shows the comparison of numerical simulations using different parameters. In Fig. 8a), $\theta_0 = 75^\circ$, $f^* = 0.10$, and the oscillation shock occurs as indicated by the changes in the normal variation curves of these coefficients. According to Fig. 7, the optimal reduced



a) $\theta_0 = 75^\circ$ $f^* = 0.10$



b) $\theta_0 = 75^\circ$ $f^* = 0.18$

Fig. 8. Comparison of numerical simulations using different parameters ($X_p/c = 1/3$, $z_0/c = 1$, $U = 2.0$ m/s, $Re = 500,000$).

Table 2. Heaving amplitude effect.

$\theta_0(^{\circ})$	z_0/c	$\overline{C_p}$	$\eta/\%$
60	0.5	0.384	24.0
60	0.7	0.493	24.9
60	1.0	0.636	26.5
60	1.2	0.668	24.6

frequency corresponding to $\theta_0 = 75^\circ$ is 0.18. When the reduced frequency is set at 0.18, the oscillation shock of the hydrodynamic characteristics of the hydrofoil disappears, and the performance of the hydrofoil is improved as shown in Fig. 8b). The maximum value of C_p in Fig. 8b) is about 5.2, and it increases by 30% compared with that in Fig. 8a). This result shows that setting the reduced frequency to be the optimal reduced frequency corresponding to the peak power cycle-averaged coefficient can eliminate the oscillation shock of the hydrodynamic characteristics of the hydrofoil, which helps to improve the hydrofoil energy-capturing efficiency.

Previous studies have shown that if the other parameters remain unchanged, the power coefficient increases with the motion amplitude of the hydrofoil [16-22]. But this tendency is not always applicable for efficiency η . The influences of heaving amplitude on C_p and η are shown in Table 2, which shows that when the heaving amplitude z_0 is below $1.0c$, efficiency η increases with heaving amplitude. Once z_0 is above $1.0c$, efficiency decreases with heaving amplitude. The reason for this behavior is that the heaving amplitude affects not only the velocity of the hydrofoil motion but also the hydrofoil swept area.

Conclusions

In this paper, based on a theoretical analysis, an unstable hydrofoil oscillation model was developed. The model contains a linear component and a rotational non-linear component of the fluid mainstream, which leads to an abrupt change phenomenon in flow velocity and pressure distribution on the hydrofoil surface as well as variation of the hydrofoil lift force, resistance, and power when the vortex generation appears.

If the vortex shedding frequency matches the hydrofoil natural frequency, it may affect hydrofoil normal operation or even damage the hydrofoil. When designing the hydrofoil oscillation energy-capturing system, variation curves of the hydrofoil instantaneous lift coefficient, instantaneous drag coefficient, instantaneous pitch moment coefficient and instantaneous power coefficient should be as smooth as possible to prevent abrupt changes in the instantaneous hydrodynamic force and to ensure reliable operation of the tidal energy power generation system.

Setting the reduced frequency to be the optimal reduced frequency corresponding to the peak power cycle-averaged coefficient can eliminate the oscillation shock and reduce the energy dissipation of the hydrofoil. The results also show that larger pitch amplitude leads to larger optimal reduced frequency corresponding to the peak power cycle-averaged coefficient.

Acknowledgements

This work is supported by National Natural Science Foundation of China (grant Nos. 51775310, 51475270, and 51305234).

References

- JOSLIN J. Evaluating environmental risks for marine renewable energy. *Sea Technology*, **57** (2), 73, **2016**.
- LI W., ZHANG H.X. Decomposition analysis of energy efficiency in China's Beijing-Tianjin-Hebei region. *Polish Journal of Environment Studies*, **26** (1), 189, **2017**.
- OUREILIDIS K.O., BAKIRTZIS E.A., DEMOULIAS C.S. Frequency-based control of islanded microgrid with renewable energy sources and energy storage. *Journal of Modern Power Systems and Clean Energy*, **4** (1), 54, **2016**.
- HARDING S.F., PAYNE G.S., BRYDEN I.G. Generating controllable velocity fluctuations using twin oscillating hydrofoils: experimental validation. *Journal of Fluid Mechanics*, **750**, 113, **2014**.
- HARDING S.F., BRYDEN I.G. Generating controllable velocity fluctuations using twin oscillating hydrofoils. *Journal of Fluid Mechanics*, **713**, 150, **2012**.
- MUNCH C., AUSONI P., BRAUN O., FARHAT M., AVELLAN F. Fluid-structure coupling for an oscillating hydrofoil. *Journal of Fluids and Structures*, **26** (6), 1018, **2010**.
- LIU Z., HYUN B.S., KIM M.R., JIN J.Y. Experimental and numerical study for hydrodynamic characteristics of an oscillating hydrofoil. *Journal of Hydrodynamics*, **20** (3), 280, **2008**.
- SATO K., TANADA M., MONDEN S., TSUJIMOTO Y. Observations of oscillating cavitation on a flat plate hydrofoil. *JSME International Journal Series B-Fluids and Thermal Engineering*, **45** (3), 646, **2002**.
- KIRKE B. Tests on two small variable pitch cross flow hydrokinetic turbines. *Energy for Sustainable Development*, **31**, 185, **2016**.
- LI H., CHANDRASHEKHAR K. Particle swarm-based structural optimization of laminated composite hydrokinetic turbine blades. *Engineering Optimization*, **47** (9), 1191, **2015**.
- FENERCIOGLU I., ZALOGLU B., YOUNG J., ASHRAF M.A., LAI J.C.S., PLATZER M.F. Flow structures around an oscillating-wing power generator. *AIAA Journal*, **52** (11), 3316, **2015**.
- MCKINNEY W., DELAURIER J. The wingmill: An oscillating-wing windmill. *Journal of Energy*, **5** (2), 109, **1981**.
- JONES K., LINDSEY K., PLATZER M. An investigation of the fluid structure interaction in an oscillating-wing micro-hydropower generator. *Physics of Atomic Nuclei*, **65** (2), 73, **2003**.
- AMIRALAEI M.R., ALIGHANBARI H., HASHEMI S.M. Flow field characteristics study of a flapping airfoil using computational fluid dynamics. *Journal of Fluids and Structures*, **27** (7), 1068, **2011**.
- AMIRALAEI M.R., ALIGHANBARI H., HASHEMI S.M. An investigation into the effects of unsteady parameters on the aerodynamics of a low Reynolds number pitching airfoil. *Journal of Fluids and Structures*, **26** (6), 979, **2010**.
- THIERY M., COUSTOLS E. URANS computations of shock-induced oscillations over 2D rigid airfoils: influence of test section geometry. *Flow Turbulence and Combustion*, **74** (4), 331, **2005**.
- THIERY M., COUSTOLS E. Numerical prediction of shock induced oscillations over a 2D airfoil: Influence of turbulence modelling and test section walls. *International Journal of Heat and Fluid Flow*, **27** (4), 661, **2006**.
- ASHRAF M.A., YOUNG J., LAI J.C.S., PLATZER M.F. Numerical analysis of an oscillating-wing wind and hydropower generator. *AIAA Journal*, **49** (7), 1374, **2011**.
- YOUNG J., LAI J.C.S. Oscillation frequency and amplitude effects on the wake of a plunging airfoil. *AIAA journal*, **42** (10), 2042, **2004**.
- BENRAMDANE S., CEXUS J.C., BOUDRAA A.O., ASTOLFI J.A. Time-frequency analysis of pressure fluctuations on a hydrofoil undergoing a transient pitching motion using Hilbert-Huang and Teager-Huang transforms. *Proceedings of the ASME Pressure Vessels and Piping Conference- Fluid-Structure Interaction*, **4**, 199, **2007**.
- GHASEMI A., OLINGER D.J., TRYGGVASON G. A nonlinear computational model of tethered underwater kites for power generation. *Journal of Fluids Engineering, Transactions of the ASME*, **138** (12), 121401, **2016**.
- GHASEMI A., OLINGER D.J., TRYGGVASON G. Computational simulation of tethered undersea kites for power generation. *Proceedings of the ASME International Mechanical Engineering Congress and Exposition*, **6B**, 50809, **2016**.
- SAGHARICHI A., MAGHREBI M.J., ARABGOLARCHEH A. Variable pitch blades: an approach for improving performance of Darrieus wind turbine. *Journal of Renewable and Sustainable Energy*, **8** (5), 053305, **2016**.
- ZHU Q., Optimal frequency for flow energy harvesting of a flapping foil. *Journal of Fluid Mechanics*, **675**, 495, **2011**.
- SHIMIZU E., ISOGAI K., OBAYASHI S. Multiobjective design study of a flapping wing power generator. *Journal of Fluids Engineering, Transactions of the ASME*, **130** (2), 021104, **2008**.
- YOUNG J., LAI J.C.S., PLATZER M.F. A review of progress and challenges in flapping foil power generation. *Progress in Aerospace Sciences*, **67**, 2, **2014**.
- XIAO Q., LIAO W., YANG S.C., PENG Y. How motion trajectory affects energy extraction performance of a biomimic energy generator with an oscillating foil. *Renewable Energy*, **37** (1), 61, **2012**.
- DUGUNDJI J. Theoretical considerations of panel flutter at high supersonic mach numbers. *AIAA Journal*, **4** (7), 1257, **1966**.
- WILSON E.L., KHALVATI M. Finite elements for the dynamic analysis of fluid-solid systems. *International Journal for Numerical Methods in Engineering*, **19** (11), 1657, **1983**.

30. GREGORY F., VARGAS L., M. LUIS. Nonlinear dynamic analysis of fluid-structure systems. *Journal of Engineering Mechanics*, **114** (2), 219, **1988**.
31. AKCABAY D.T., YOUNG Y.L. Influence of cavitation on the hydroelastic stability of hydrofoils. *Journal of Fluids and Structures*, **49**, 170, **2014**.
32. KAPERAKI A.E., BELIBASSAKIS K.A., PAPATHANASIOU T.K. Time-domain, shallow-water hydroelastic analysis of VLFS elastically connected to the seabed. *Marine Structures*, **48**, 33, **2016**.